


**Please cite the Published Version**

Wnag, Ping, Guangyao, Xu, Peng, Yong, Zhou, Jian  and Peng, Yuji (2025) Smagorinsky Constant Distribution and Turbulent Energy Dissipation in High Reynolds-Number Cavity Flow. *Physics of Fluids*, 37 (6). 065158 ISSN 1070-6631

**DOI:** <https://doi.org/10.1063/5.0274909>

**Publisher:** AIP Publishing

**Version:** Accepted Version

**Downloaded from:** <https://e-space.mmu.ac.uk/640415/>

**Usage rights:**  [Creative Commons: Attribution 4.0](https://creativecommons.org/licenses/by/4.0/)

**Additional Information:** This is an author accepted manuscript of an article published in *Physics of Fluids*, by AIP Publishing. This version is deposited with a Creative Commons Attribution 4.0 licence [<https://creativecommons.org/licenses/by/4.0/>], in accordance with Man Met's Research Publications Policy. The version of record can be found on the publisher's website.

**Enquiries:**

If you have questions about this document, contact [openresearch@mmu.ac.uk](mailto:openresearch@mmu.ac.uk). Please include the URL of the record in e-space. If you believe that your, or a third party's rights have been compromised through this document please see our Take Down policy (available from <https://www.mmu.ac.uk/library/using-the-library/policies-and-guidelines>)

1 **Smagorinsky Constant Distribution and Turbulent Energy Dissipation in High**  
2 **Reynolds-Number Cavity Flow**

3 Ping Wang<sup>1</sup>(王平), Guangyao Xu<sup>1</sup>(许光耀), Yong Peng<sup>2\*</sup>(彭勇), Jianguo Zhou<sup>3</sup>(周  
4 建国), Yuji Peng<sup>1</sup>(彭宇骥)

5 <sup>1</sup> College of Water Resources and Architectural Engineering, Northwest A&F University,  
6 Yangling, Shaanxi 712100, China. Email: 1179424728@foxmail.com

7 <sup>2</sup> College of Water Resources and Architectural Engineering, Northwest A&F University,  
8 Yangling, Shaanxi 712100, China. Email: [pengyongscu@foxmail.com](mailto:pengyongscu@foxmail.com)

9 <sup>3</sup> Department of Computing & Mathematics, Manchester Metropolitan University, Manchester  
10 M1 5GD, UK, Email: J.Zhou@mmu.ac.uk

11 \* Corresponding author: Yong Peng, [pengyongscu@foxmail.com](mailto:pengyongscu@foxmail.com)  
12

13 **Abstract:** This study experimentally investigates lid-driven cavity flow at high  
14 Reynolds numbers ( $Re = 3 \times 10^5$  to  $1 \times 10^6$ ) using Particle Image Velocimetry (PIV). The  
15 spatial distribution of root mean square (RMS) velocity, turbulent kinetic energy  
16 dissipation rate, and the Smagorinsky constant is analyzed to reveal key turbulence  
17 characteristics. Results show that: (1) The RMS velocity increases significantly in the  
18 near-wall region with Reynolds number, reaching a peak of 0.43 m/s on the downstream  
19 near-wall surface at  $Re = 1 \times 10^6$ , while remaining below 0.1 m/s in the core region due  
20 to flow stability suppressing turbulence fluctuations; (2) The turbulent kinetic energy  
21 dissipation rate exhibits significant spatial nonuniformity near the wall, with a peak  
22 value of 0.6 at  $Re = 1 \times 10^6$ ; as Reynolds number increases, high dissipation regions  
23 extend further into the cavity interior and evolve into multiscale fragmented structures;  
24 (3) The Smagorinsky constant is close to zero near the cavity wall, gradually increases  
25 with distance from the wall, reaches a maximum, and then decreases to zero at the

26 cavity center. As Reynolds number increases, the overall Smagorinsky constant  
27 increases, with a more significant rise in its maximum value at higher Reynolds  
28 numbers, indicating stronger eddy viscosity. These findings provide experimental  
29 insights for improving the nonuniform parameterization in eddy viscosity models for  
30 large-eddy simulations.

31 **Keywords:** Lid-driven cavity flow; High Reynolds number; Particle Image Velocimetry;  
32 Large Eddy Simulation; Smagorinsky constant

### 33 **1. Introduction**

34 Turbulence is a complex and pervasive phenomenon found in both natural and  
35 engineering systems, presenting significant challenges for numerical simulations in  
36 fluid dynamics due to its multi-scale vortex interactions and energy cascade  
37 characteristics (Smagorinsky, 1963). In practical application such as atmospheric  
38 circulation, aircraft aerodynamics, and chemical reactor flows, traditional numerical  
39 methods must balance accuracy and computational efficiency. While Direct Numerical  
40 Simulation (DNS) can fully resolve the turbulence spectrum (Ghia et al., 1982), it  
41 becomes prohibitively expensive at high Reynolds numbers. On the other hand,  
42 Reynolds-Averaged Navier-Stokes (RANS) methods, which rely on time-averaged  
43 equations to reduce computational costs (Pan and Acrivos, 1967), fail to capture  
44 transient turbulence fluctuations. Large Eddy Simulation (LES) has emerged as the  
45 leading approach, as it directly resolves large-scale vortices while modeling the effects  
46 of unresolved small-scale turbulence (Germano et al., 1991). However, the main

47 challenge in LES lies in the development of Subgrid-Scale (SGS) models and the  
48 optimization of their empirical parameters to improve predictive capabilities. The  
49 classical Smagorinsky model defines a nonlinear relationship between subgrid-scale  
50 stress and strain rate tensors based on the hypothesis of eddy viscosity, where the  
51 empirical constant  $C_s$  directly influences turbulence energy dissipation rate (Wang et al.,  
52 2020). Early studies demonstrated success in homogeneous isotropic turbulence using  
53 a fixed  $C_s$  value (ranging from 0.1 to 0.18) (Geurts et al., 1999), but faced significant  
54 limitations in more complex flow scenarios. Malik et al. (2016) found that, while the  
55 Shear-Improved Smagorinsky Model (SISM) with  $C_s=0.18$  could predict friction  
56 velocity in plane channel flow with less than 3% error compared to reference DNS data,  
57 it struggled to capture transient flow characteristics effectively when applied to  
58 complex unsteady flows. Dallali et al. (2015) emphasized the importance of selecting  
59 an appropriate  $C_s$  value for accurate turbulence simulations in sediment transport  
60 studies. Collectively, these findings highlight the inherent limitations of the fixed  $C_s$   
61 model in non-homogeneous and unsteady flows. To improve model adaptability, the  
62 dynamic Smagorinsky model optimizes the  $C_s$  value in real-time using double filtering  
63 (Germano et al., 1991), enhancing accuracy in shear flows (Vreman et al., 2004).  
64 However, it faces challenges with parameter oscillations at extreme Reynolds numbers,  
65 and deficiencies in the near-wall region persist. Hybrid models, such as Detached Eddy  
66 Simulation (DES) combined with data-driven methods, provide new solutions. Beck et  
67 al. (2019) demonstrated that, with  $C_s = 0.12$ , a hybrid model incorporating an Artificial  
68 Neural Network (ANN) closure term can stably simulate Decaying Homogeneous

69 Isotropic Turbulence (DHIT), significantly outperforming the standard Smagorinsky  
 70 model. Despite these advantages, fixed  $C_s$  coefficients still restrict adaptability, making  
 71 it difficult to capture the dynamic characteristics of high Reynolds number flows. The  
 72 limitations of the fixed  $C_s$  model become more apparent in engineering practice. Bianco  
 73 et al. (2016) found that , with  $C_s = 0.1$  in the double-loop vortex tube heat transfer  
 74 simulation, the prediction of heat transfer performance was biased, and this bias could  
 75 not be fully corrected even with grid refinement. Piomelli and Balaras (2002) pointed  
 76 out that in strong shear flows,  $C_s$  must be adjusted from 0.10 in the core flow region to  
 77 0.05 near the wall. This spatially varying adjustment not only increases computational  
 78 complexity but also leads to excessive suppression of turbulence fluctuations in the  
 79 near-wall region. Notably, the WALE model (Nicoud and Ducros, 1999) introduces the  
 80 square of the velocity gradient tensor to construct subgrid viscosity, and its constant  $C_w$   
 81 is optimized in the range of 0.55-0.60 for simulating decaying turbulence. However,  
 82 compared to the dynamic  $C_s$  adjustment strategy, it remains constrained by the inherent  
 83 limitation of a fixed constant.. More recently, de Crouy-Chanel et al. (2024) calibrated  
 84 the VMS-Smag model ( $C_s = 0.41$ ) using the remeshed vortex method, achieving optimal  
 85 accuracy in simulating Taylor-Green vortices. Nonetheless, its applicability in wall-  
 86 bounded flows still requires further validation. High Reynolds number lid-driven cavity  
 87 flow, a common flow pattern in applications like aircraft engine cooling channels and  
 88 building ventilation systems (Spalart et al., 2006), exhibits characteristics of strong  
 89 inertial dominance, complex multi-scale vortex interactions, and poorly understood  
 90 energy dissipation mechanisms. Existing studies often use a fixed  $C_s = 0.17$  or empirical

91 damping functions to modify near-wall dissipation (Lund et al., 1998), but they face  
92 dual challenges in practical applications. First, the fixed  $C_s$  value leads to excessive  
93 suppression of turbulence fluctuations in the wall region (Sardina et al., 2012), which  
94 affects the physical realism of vortex evolution. Second, the wall damping function is  
95 difficult to accurately define accurately in complex geometries (Vreman et al., 2004).  
96 Although dynamic models improve the accuracy of shear flow simulations through  
97 local parameter optimization (Germano et al., 1991), the distribution of  $C_s$  values and  
98 their dynamic correlation with flow field characteristics in high Reynolds number lid-  
99 driven cavity flows have yet to be revealed. Recent research shows that most studies on  
100 cavity flows focus on low to medium Reynolds numbers (Abdi et al., 2021; Carlos et  
101 al., 2021; Trong et al., 2020), and systematic experimental studies on high Reynolds  
102 number ( $Re \geq 1 \times 10^5$ ) cavity flow are still scarce (Bouffanais et al., 2007; Wang et al.,  
103 2025; Samantaray et al., 2020). Particularly under the high Reynolds number condition  
104 of  $Re = 1 \times 10^5$ , the distribution of  $C_s$  values and their dynamic correlation with flow field  
105 features remain unexplored, lacking sufficient experimental research and in-depth  
106 exploration.

107 To address these challenges, this study systematically investigates high Reynolds  
108 number flow in a 0.25m lid-driven cavity at  $Re = 3 \times 10^5$  to  $1 \times 10^6$ . Using PIV to obtain  
109 transient flow field data, it analyzes the spatiotemporal evolution of  $C_s$  values and  
110 develops a model linking them to local turbulence kinetic energy dissipation  
111 mechanisms. This approach more accurately captures turbulence's dynamic evolution  
112 and multi-scale coupling effects, overcoming the limitations of the traditional fixed  $C_s$

113 models. The results provide physical-driven optimization guidelines for dynamic  
114 subgrid models and advance turbulence simulations from empirical corrections to a  
115 mechanism-driven paradigm, laying the theoretical foundation for refined prediction of  
116 high Reynolds number complex flows.

## 117 2. Experimental Setup and Methods

### 118 2.1 Experimental Setup

119 The experiment was conducted in a recirculating cubic cavity flow system, with  
120 the cavity dimensions being 0.25 m in length, width, and height, as shown in Figure 1.  
121 The top cover of the cavity is driven by a belt that moves the fluid, with the belt speed  
122 adjustable to control the Reynolds number. To ensure stable water volume inside the  
123 cavity, unaffected by the driving mechanism, a large water tank was installed at the  
124 outer edge of the cavity's top cover. The belt is submerged in the water tank, ensuring  
125 that the water flow is not reduced due to fluid loss outside the tank. During the  
126 experiment, the belt speed was adjusted to bring the Reynolds number close to the  
127 preset value. Tracer particles with an appropriate concentration were added to the water,  
128 and after waiting for 10-15 minutes to allow the flow system to stabilize, the laser was  
129 adjusted to illuminate the tracer particles along the middle plane of the cavity,  
130 specifically at  $X=0$ , as shown in Figure 1. The belt rotates along the x-direction of the  
131 cavity. High-speed cameras were used to capture and store experimental images. The  
132 experiment was repeated for different Reynolds numbers, adjusting the test conditions  
133 to obtain flow field data for varying Reynolds numbers.

134 This experiment utilized a classical multi-channel 2D2C PIV system for flow field  
135 measurements. The system consisted of a high-speed frame-straddling camera, a  
136 continuous laser, a synchronizer, and a computer. The high-speed camera used was the  
137 M220M model produced by Zhongke JunDa Vision Technology Co., Ltd., equipped  
138 with a 50 mm F1.4 lens, providing a maximum image resolution of  $1920 \times 1080$  pixels  
139 and a maximum frame rate of 1000 frames per second. For actual measurements, the  
140 image resolution was set to  $1024 \times 1024$  pixels to balance computational accuracy and  
141 image processing efficiency. The PIV data processing employed the classical cross-  
142 correlation algorithm, combined with a multi-level grid iterative image deformation  
143 method (Image Deformation Algorithm) to improve image processing accuracy.  
144 Additionally, sub-pixel precision localization techniques were used to further optimize  
145 the displacement calculation accuracy. To ensure smooth velocity field calculations, the  
146 window overlap rate was set to 25%. The laser source used was a continuous 532 nm  
147 green laser with a power of 8 W, providing stable illumination intensity. Hollow glass  
148 microspheres with a diameter of 10  $\mu\text{m}$  and a density of 1.1  $\text{g/cm}^3$ , closely matching  
149 that of water, were chosen as tracer particles due to their excellent flow-following  
150 characteristics, allowing for precise tracking of fluid motion. Image acquisition was  
151 performed using the "JunDa High-Tech High-Speed Image Acquisition System V1.0"  
152 software developed by Zhongke JunDa Vision Technology Co., Ltd. (Huang et al.,  
153 2019). This system efficiently synchronized the laser and camera, ensuring accurate  
154 continuous image capture. With this setup, the experiment successfully observed typical  
155 vortex structures within the neutral-plane flow field, including the primary vortex (PV),



156 downstream secondary vortex (DSV), upstream secondary vortex (USV), and upstream  
157 unsteady vortex (UUV), along with other characteristic flow structures.

158 The Reynolds numbers measured in this study are  $3 \times 10^5$ ,  $5 \times 10^5$ ,  $7 \times 10^5$ , and  $1 \times 10^6$ .

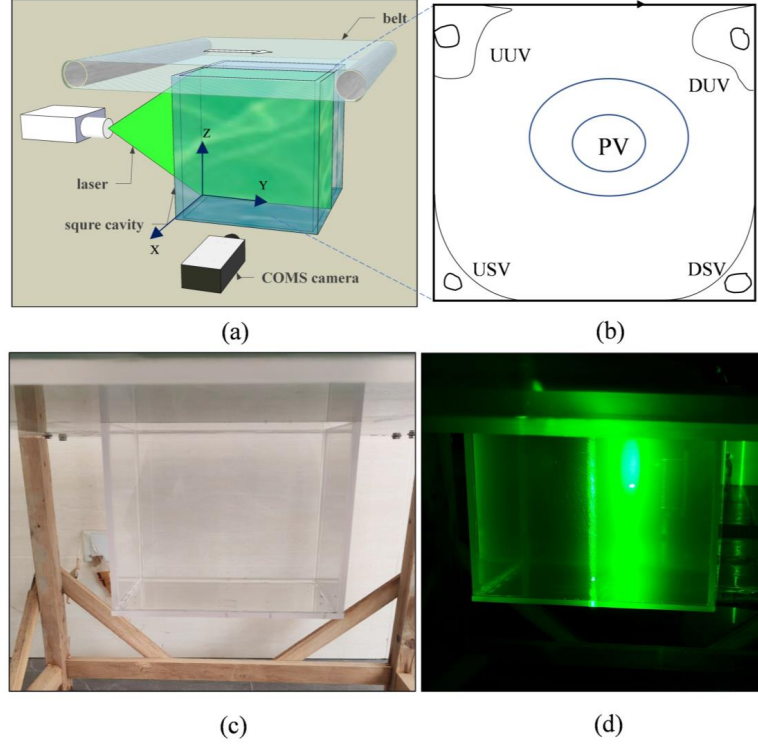
159 The Reynolds number is defined as  $Re = UL/\nu$ , where  $\nu$  is the kinematic viscosity and  $L$   
160 is the length of the cavity. The required driving velocity can be calculated using this  
161 formula.

162 In the experiments conducted within the Reynolds number range of  $Re = 5 \times 10^5$  to  
163  $1 \times 10^6$ , the velocity field was subjected to uncertainty quantification analysis using PIV.

164 Based on the time series statistics of multiple instantaneous velocity fields for each  
165 condition, the spatially averaged standard deviation ( $\sigma_{avg}$ ) ranged from 0.0263 to 0.0516  
166 m/s, reflecting the variation in turbulence fluctuation intensity with Reynolds number.

167 The maximum relative error ( $\varepsilon_{max}$ ) is below 1.5%. The PIV system was calibrated by  
168 the National Institute of Metrology, and the system's accuracy remains stable, with a  
169 relative error of -0.42% to -0.58% and repeatability  $< 0.33\%$ , ensuring the reliable  
170 accuracy of the high Reynolds number experimental results.

171



172

173 Fig. 1. Lid driven cavity. (a) Schematic of the experimental setup.(b) Vortex structure  
174 diagram. (c) Laboratory square cavity. (d) PIV imaging of the middle plane.

## 175 2.2 Large Eddy Simulation Governing Equations and Subgrid-Scale Stress

### 176 2.2.1 Governing Equations of Large Eddy Simulation

177 In LES, a spatial filtering operation decomposes the velocity field into a resolved  
178 large-scale component and an unresolved small-scale fluctuating component, which  
179 represents the subgrid-scale fluctuations.  $u_i = \bar{u}_i + u_i'$  (1)

180 where  $u_i$  represents the resolved large-scale low-pass filtered velocity, and  $\bar{u}_i$   
181 represents the unresolved small-scale residual fluctuations  $u_i'$ .

182 Assuming that the filtering process and the differentiation process can be  
 183 interchanged, filtering the Navier-Stokes equations leads to the governing equations of  
 184 LES.

$$185 \quad \frac{\partial \bar{u}_i}{\partial t} + \frac{\partial \bar{u}_i \bar{u}_j}{\partial x_j} = -\frac{1}{\rho} \frac{\partial \bar{p}}{\partial x_i} + \nu \frac{\partial^2 \bar{u}_i}{\partial x_j \partial x_j} \quad (2)$$

$$186 \quad \frac{\partial \bar{u}_i}{\partial x_i} = 0 \quad (3)$$

187 Let  $\bar{u}_i \bar{u}_j = \overline{u_i u_j} + (\overline{u_i u_j} - \overline{u_i u_j})$ . The term  $-(\overline{u_i u_j} - \overline{u_i u_j})$  is defined as the SGS, then  
 188 Equation (2) can be rewritten as:

$$189 \quad \frac{\partial \bar{u}_i}{\partial t} + \frac{\partial \bar{u}_i \bar{u}_j}{\partial x_j} = -\frac{1}{\rho} \frac{\partial \bar{p}}{\partial x_i} + \nu \frac{\partial^2 \bar{u}_i}{\partial x_j \partial x_j} - \frac{\bar{\tau}_{ij}}{\partial x_j} \quad (4)$$

190 In the equation,  $\bar{\tau}_{ij} = \overline{u_i u_j} - \overline{u_i u_j}$  represents the SGS stress. To perform large eddy  
 191 simulation, it is essential to construct a closure model.

## 192 2.2.2 Subgrid-Scale Stress Model in Large Eddy Simulation

193 The most widely used subgrid-scale model is the Smagorinsky eddy viscosity  
 194 model (Shui et al., 2022).

$$195 \quad \bar{\tau}_{ij} = (\overline{u_i u_j} - \overline{u_i u_j}) = 2(C_s \Delta)^2 \bar{S}_{ij} (2\bar{S}_{ij} \bar{S}_{ij})^{1/2} - \frac{1}{3} \tau_{kk} \delta_{ij} \quad (5)$$

196 Here,  $\Delta$  is the filter size, the subgrid-scale viscosity  $\nu = (C_s \Delta)^2 (2\bar{S}_{ij} \bar{S}_{ij})^{1/2}$ , and  $C_s$  is the  
 197 Smagorinsky constant, which corresponds to the mixing length.

## 198 2.3 Methods for Computing the Smagorinsky Constant

199 The distribution of the  $C_s$  in the SGS energy flux and turbulence energy dissipation  
 200 rate requires approach to compute the dissipation rate for closing the corresponding  
 201 equations. The following section describes the formulas for calculating turbulence  
 202 kinetic energy dissipation and the  $C_s$  in Large Eddy Simulation, as well as other

203 methods for computing turbulence kinetic energy dissipation.

### 204 2.3.1 Smagorinsky Constant in Large Eddy Simulation

205 To study LES from the energy perspective, multiply both sides of equation (4) by  
206 the velocity  $\overline{u_i}$  and simplify it, resulting in the kinetic energy balance equation:

$$207 \quad \frac{\partial \overline{q}^2}{\partial t} + \overline{u_i} \frac{\partial \overline{q}^2}{\partial x_j} = \frac{\partial}{\partial x_j} (-\overline{p u_j} + \frac{\partial \overline{q}^2}{\partial x_j} - \tau_{ij} \overline{u_i}) - \nu \frac{\partial \overline{u_i}}{\partial x_j} \frac{\partial \overline{u_i}}{\partial x_j} + 2 \tau_{ij} \overline{S_{ij}} \quad (6)$$

208 The left-hand side of the equation represents the rate of change of kinetic energy with  
209 time and the convective transport term. The right-hand side includes work done by  
210 pressure, viscous dissipation, work done by subgrid-scale stress, and the vortex  
211 dissipation term representing the transfer of large-scale turbulence kinetic energy to  
212 small scales. In Large Eddy Simulation, the turbulence kinetic energy dissipation rate  
213 can be approximately represented by the SGS energy dissipation rate (Meneveau and  
214 Katz, 2000).

$$215 \quad \varepsilon \approx \langle \varepsilon_{SGS} \rangle = -2 \langle \tau_{ij} \overline{S_{ij}} \rangle \quad (7)$$

216 In the Smagorinsky model, the subgrid-scale stress is given by  $\tau_{ij} = -C_s^2 \Delta^2 |\overline{S}| \overline{S_{ij}}$ .

### 217 2.3.2 Calculation Methods for Dissipation Rate $\varepsilon$

#### 218 (1) Dimensional Analysis Method

219 In the study of turbulence dissipation rate, the dimensional analysis method  
220 provides a way to express it using the Taylor scale and turbulent velocity. The  
221 turbulence dissipation rate can be expressed as:

$$222 \quad \varepsilon = 15 \nu \frac{u'^2}{\lambda^2} \quad (8)$$

223 Here,  $\lambda$  represents the Taylor scale. According to the balance turbulence scales

224 (Konstantinos, 2022; Rubinstein and Clark,2017), equation (8) can be further  
 225 transformed as follows:

$$226 \quad \varepsilon = A \frac{u^3}{l} \quad (9)$$

227 Here,  $l$  represents the integral scale, and  $A$  is a constant close to 1.

## 228 (2) Large Eddy PIV Method

229 The velocity field obtained using PIV is low-pass filtered, similar to LES. As a  
 230 result, only larger scales flow structures are resolved, with vortices smaller than the  
 231 filtering scale are excluded. In high Reynolds number flow fields, turbulence kinetic  
 232 energy is generated at the integral scale and dissipates near the Kolmogorov scale, with  
 233 energy conservation between the two (Sikiö et al., 2018). An inertial subrange exists  
 234 between these scales, where energy is transferred from larger to smaller scales without  
 235 being generated or dissipated (Buaria and Sreenivasan, 2020). Therefore, when  
 236 estimating the dissipation rate, it is sufficient to calculate the energy flowing through  
 237 the inertial subrange, without needing to precisely resolve the Kolmogorov scale.

238 Sheng et al. (2000) proposed the Large Eddy PIV method, which uses data  
 239 obtained through PIV measurements to directly calculate the turbulence dissipation rate.

240 The point velocity in the actual fluid can be represented by the velocity measured using  
 241 PIV:

$$242 \quad u_i = U_i - \Phi(U_i) + \frac{1}{2!}\Phi^2(U_i) - \frac{1}{3!}\Phi^3(U_i) + \dots \quad (10)$$

243 where,  $\Phi(U_i) = (a_1 \partial^2 / \partial x_1^2 + a_2 \partial^2 / \partial x_2^2 + a_3 \partial^2 / \partial x_3^2)U_i$ , here  $U_i$  is the velocity obtained using  
 244 PIV, and  $a_1, a_2, a_3$  are constants related to the low-pass filtering width in the three

245 directions. These constants are typically expressed in a unified form as:

$$246 \quad a_i = \frac{\Delta_i^2}{8}, i = 1, 2, 3, \quad (11)$$

247 Here,  $\Delta_i$  is the filter width, and substituting it into the equation gives:

$$248 \quad u_i = U_i - \frac{\Delta^2}{8} L^2 \bar{\nabla}_i + \frac{\Delta^4}{1024} \nabla^4 U_i + \dots \quad (12)$$

249 Based on dimensional analysis, the second term in equation (12) is approximately  
 250 related to  $\Delta^2 / l^2$ , where  $l$  is the integral scale and  $\Delta$  is the filter scale. Since  $\Delta \ll l$ ,  
 251 there is a magnitude difference, allowing the second term and all subsequent terms to  
 252 be approximated as 0, leading to:

$$253 \quad \langle u_i \rangle \approx \langle U_i \rangle$$

$$254 \quad u_i' \approx U_i - \langle U_i \rangle \quad (13)$$

$$255 \quad \langle u_i' u_j' \rangle \approx U_i U_j - \langle U_i \rangle \langle U_j \rangle$$

256 The filtered Navier-Stokes equations can be represented using the PIV  
 257 measurement data as follows:

$$258 \quad \frac{\partial U_i}{\partial x_i} = 0 \quad (14)$$

$$259 \quad \frac{\partial U_i}{\partial t} + \frac{\partial (U_i U_j)}{\partial x_j} = -\frac{\partial P}{\partial x_j} + \nu \frac{\partial^2 U_i}{\partial x_j^2} - \frac{\partial \tau_{ij}}{\partial x_j} \quad (15)$$

260 Correspondingly, the energy balance equation can be expressed as follows:

$$261 \quad \frac{\partial \bar{q}^2}{\partial t} + U_j \frac{\partial \bar{q}^2}{\partial x_j} = \frac{\partial}{\partial x_j} (-P U_j + \nu \frac{\partial \bar{q}^2}{\partial x_j} - \tau_{ij} U_i) - \nu \frac{\partial U_i}{\partial x_j} \frac{\partial U_i}{\partial x_j} + 2 \tau_{ij} \bar{S}_{ij} \quad (16)$$

262 where  $\bar{S}_{ij} = \frac{1}{2} (\frac{\partial U_i}{\partial x_j} + \frac{\partial U_j}{\partial x_i})$  denotes the strain rate tensor derived from measurements.

263 The last term in the equation represents the viscous term. It indicates the energy  
 264 transferred from the resolved scale to the small scales, and also represents the SGS  
 265 energy flux. The momentum transport can be expressed through this energy flux:

$$\varepsilon \approx \langle \varepsilon_{SGS} \rangle = -2 \langle \tau_{ij} \overline{S_{ij}} \rangle \quad (17)$$

### 2.3.3 Smagorinsky Constant Calculation Formula

The  $C_s$  is calculated by closing the equations using the dimensional analysis method and the Large Eddy PIV method. The two equations are solved simultaneously:

$$\varepsilon = A \frac{u'^3}{l} = -2 \langle \tau_{ij} \overline{S_{ij}} \rangle = 4 C_s^2 \Delta^2 \langle (\overline{S_{ij}} \overline{S_{ij}})^{3/2} \rangle \quad (18)$$

Here,  $u'$  is the root-mean-square velocity, and  $\Delta$  is the filter width. The following analyzes each term in the equation.

#### (1) Root Mean Square Velocity

The Root Mean Square (RMS) Velocity quantifies the magnitude of velocity fluctuations in turbulent flows, serving as a key metric for characterizing turbulence intensity. The calculation formula is as follows:

$$u_{ij}' = (\overline{u_{ij}^2})^{\frac{1}{2}} = \sqrt{\frac{1}{N} \sum_{n=1}^N (u_{ij})^2} \quad (19)$$

In PIV experiments, the velocity field measurements typically include instantaneous velocity and time-averaged velocity. The velocity obtained from PIV measurements can be expressed as:

$$u_{ij}' = (\overline{u_{ij}^2})^{\frac{1}{2}} = \sqrt{\frac{1}{N} \sum_{n=1}^N (U_{ij})^2} \quad (20)$$

where  $U_{ij}$  is the time-averaged velocity obtained from PIV measurements. Significant fluctuations in flow velocity and the potential periodic variations make it insufficient to simply average a large amount of long-term data when processing PIV results. In this experiment, to obtain a more accurate time-averaged velocity, we employed a local averaging method. For each time  $t$ , the data from 10 time steps before and after  $t$  are selected, and the average velocity over those 21 time steps is calculated to represent the average velocity at  $t$ . This method effectively reduces the impact of random fluctuations in instantaneous velocity, making the resulting time-averaged velocity more representative, resulting in a more accurate calculation of the root mean square

291 velocity.

## 292 (2) Integral Length Scale $l$

293 The integral length scale is an important parameter for describing turbulence  
294 characteristic (Arun et al., 2023), and is commonly represented by the integral of the  
295 autocorrelation coefficient of the velocity between two arbitrary points. The  
296 autocorrelation function  $R(\Delta r)$  reflects the correlation between the velocities at two  
297 points, and is expressed as:

$$298 \quad R(\Delta r) = \frac{\overline{u_i'(x,t)u_i'(x+\Delta r,t)}}{\sqrt{\overline{u_i'^2(x,t)u_i'^2(x+\Delta r,t)}}} \quad (21)$$

299 Here,  $R(\Delta r)$  represents the autocorrelation coefficient between two points separated  
300 by a distance  $\Delta r$ , and  $u_i'$  represents the fluctuating velocity, which is the instantaneous  
301 velocity minus the mean velocity. The superscript indicates the time average over  
302 different time scales. By subtracting the time-averaged velocity from the instantaneous  
303 velocity at each time step, the fluctuating velocity is obtained, and the autocorrelation  
304 coefficient is computed from these fluctuating velocities.

305 The calculation formula for the integral length scale  $l$  is:

$$306 \quad l = \int_0^{\Delta r_{\max}} R(\Delta r) d\Delta r \quad (22)$$

307 in which,  $\Delta r_{\max}$  is the distance where the autocorrelation function first equals 0. In  
308 theory, when the two points are at a distance of 0, the autocorrelation function equals 1;  
309 when the distance approaches infinity, the autocorrelation function equals 0.

## 310 (3) Turbulence Kinetic Energy Dissipation Rate Using the Scale Similarity Method

311 Dimensional analysis is an important method in the study of turbulence dissipation  
312 rate. Using equation (9) to calculate the turbulence kinetic energy dissipation rate helps  
313 to understand the characteristics of turbulent energy dissipation.

## 314 (4) Strain rate tensor

315 The strain rate tensor is expressed as:

$$316 \quad \bar{S}_{ij} = \frac{1}{2} \left( \frac{\partial U_j}{\partial x_i} + \frac{\partial U_i}{\partial x_j} \right) \quad (23)$$



317 The experiment uses two-dimensional PIV to observe the flow field, and the flow  
 318 velocity within the plane has been determined. Therefore,  $\bar{S}_{ij}$  for  $i, j = 1, 2$  is,

$$\begin{aligned}\bar{S}_{11} &= \frac{\partial U_1}{\partial x_1} \\ \bar{S}_{12} = \bar{S}_{21} &= \frac{1}{2} \left( \frac{\partial U_1}{\partial x_2} + \frac{\partial U_2}{\partial x_1} \right) \\ \bar{S}_{22} &= \frac{\partial U_2}{\partial x_2}\end{aligned}\tag{24}$$

### 320 3.Results and Discussion

#### 321 3.1 Root Mean Square Velocity

##### 322 3.1.1 Centerline Flow Velocity

323 Figure 2 shows the distribution of the RMS velocity along the centerline of the  
 324 cavity. Experimental analysis reveals significant differences in the distribution of RMS  
 325 velocity along the cavity centerline, particularly between the near-wall region and the  
 326 primary vortex core region. In the near-wall region, both  $u_{rms}$  and  $v_{rms}$  reach their  
 327 maximum values, with  $u_{rms}$  at the bottom wall increasing from 0.19 m/s at  $Re = 3 \times 10^5$   
 328 to 0.35 m/s at  $Re = 7 \times 10^5$ . As the Reynolds number increases, particularly in the near-  
 329 wall region, the values of  $u_{rms}$  and  $v_{rms}$  increase significantly. Specifically,  $v_{rms}$  reaches  
 330 its peak near the downstream wall; at  $Re = 5 \times 10^5$ , the peak value at the upstream wall  
 331 is 0.19 m/s, while at the downstream wall, it is 0.24 m/s. The peak at the downstream  
 332 wall is slightly higher than at the upstream, indicating that turbulence fluctuations are  
 333 most intense in this region. This trend is consistent with the experimental data of Prasad  
 334 and Koseff (1989).

335 However, near the wall (at  $x = 0$  or  $y = 0$ ), due to flow resistance and the enhanced

336 end-wall effect, the RMS velocity quickly decays to nearly zero. The RMS velocity in  
337 the primary vortex core region (at  $x = 0.5$  or  $y = 0.6$ ) is significantly lower than in the  
338 near-wall region, as the main vortex structure suppresses turbulent fluctuations, and the  
339 RMS velocity in this region is less influenced by changes in Reynolds number. At high  
340 Reynolds numbers, the end-wall effect increases, leading to energy loss due to high-  
341 frequency fluctuations in the boundary layer, and reduced momentum redistribution,  
342 which decreases the velocity in the primary vortex core. In contrast, in the near-wall  
343 region, the RMS velocity rises rapidly due to the enhanced wall shear stress and  
344 turbulent intensity. These factors together cause a significant increase in RMS velocity  
345 near the wall. As the Reynolds number increases, the turbulence shear effect in the near-  
346 wall region intensifies, exacerbating boundary layer instability and causing turbulent  
347 kinetic energy accumulates, further increasing the fluctuation velocity. However, in the  
348 primary vortex core, due to the limited turbulence energy transport and lower  
349 momentum redistribution efficiency, the velocity distribution remains relatively stable.

350 The results of this study align with the findings of Samantaray and Das (2019) and  
351 Padilla et al. (2005) regarding low Reynolds number cavity flows, where the RMS  
352 velocity is higher in the near-wall region and lower in the primary vortex core. At  $Re =$   
353 10000, the RMS velocity in the primary vortex region is smaller compared to the peak  
354 value at the wall, but the difference is relatively small (Samantaray et al., 2020). This  
355 is because at low Reynolds numbers, viscous effects dominate, and the turbulence  
356 characteristics in the primary vortex region and the near-wall region are more similar.  
357 However, in high Reynolds number flows ( $Re = 3 \times 10^5$  to  $Re = 10^6$ ), the RMS velocity

358 in the primary vortex region is significantly lower than the peak value at the wall, with  
359 a larger difference. This is because in high Reynolds number flows, inertial forces  
360 dominate the evolution of turbulence, and the shear effects in the primary vortex region,  
361 which is far from the wall, are weaker, leading to lower turbulent fluctuation intensities.  
362 Meanwhile, in the wall region, turbulence intensity is higher due to stronger wall shear  
363 effects.

364 In high Reynolds number flows ( $Re = 3 \times 10^5$  to  $7 \times 10^5$ ), the velocity difference  
365 between the left and right wall is smaller, indicating that the flow has entered a fully  
366 developed turbulent state, and intense turbulent fluctuations promote lateral momentum  
367 exchange, reducing local flow differences between the two walls. This contrasts with  
368 the low Reynolds number flows, where viscous effects are predominant. In low  
369 Reynolds number conditions, the flow near the walls is significantly influenced by local  
370 vortex structures, leading to greater velocity differences. Moreover, compared to the  
371 research by Samantaray et al. (2004) on square lid-driven cavities, although their  
372 experimental Reynolds numbers were lower ( $Re = 1000$  to  $15000$ ), the variation of  
373 RMS velocity with Reynolds number showed consistent trends: as Reynolds number  
374 increased, turbulence intensity increased, and RMS velocity near solid boundaries  
375 significantly increased, while the RMS velocity in the cavity center was less influenced  
376 by changes in Reynolds number. This study further confirms that at high Reynolds  
377 numbers, the fluctuation velocity in the near-wall region increases significantly, while  
378 the core region exhibits weak dependence on Reynolds number due to flow stability  
379 limitations.

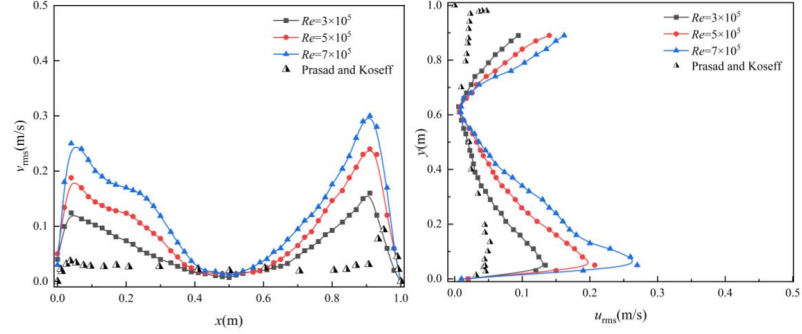
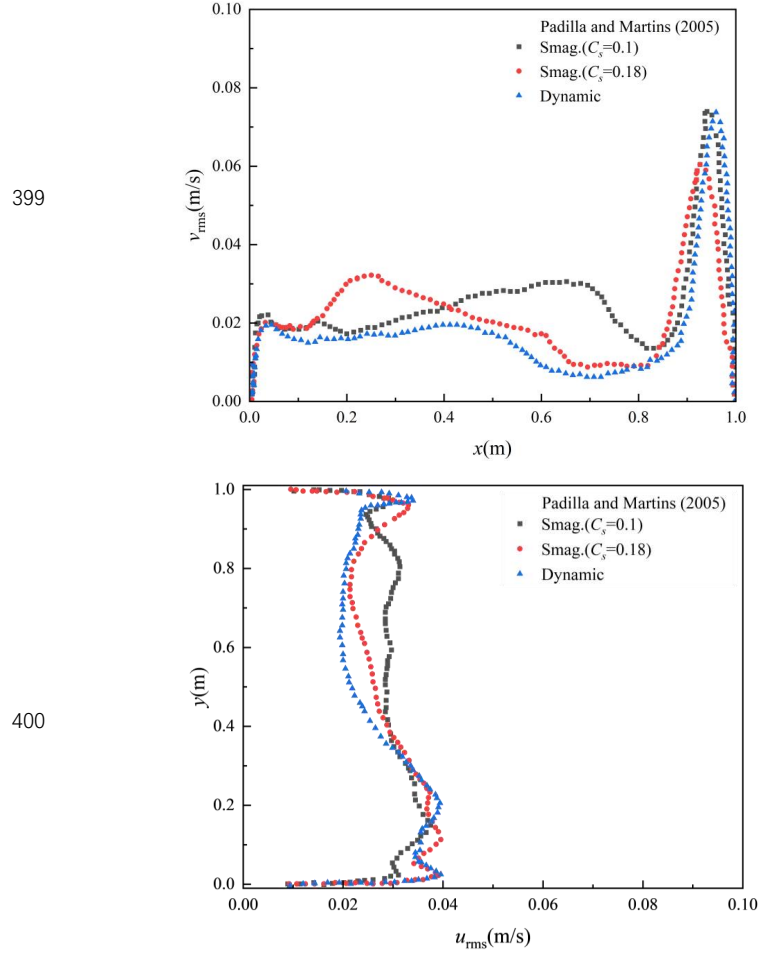


Figure 2: Root Mean Square Velocity along the Centerline , including  $u_{rms}$  and  $v_{rms}$

Regarding the two components of RMS velocity, Padilla and Martins (2005) found that when using the Smagorinsky subgrid model with a constant  $C_s = 0.1$ , the peak value near the wall was lower than that near the primary vortex, with  $v_{rms}$  reaching 0.03 m/s near the primary vortex. Similarly, at  $C_s = 0.18$ , the peak velocity at  $x = 0.25$  reached 0.32 m/s, which was significantly higher than the value near the left wall, indicating higher turbulence viscosity, which led to poor velocity statistics. As shown in Fig. 3, when using the dynamic subgrid model, the RMS velocity near the vortex center was lower than the velocity at the two side walls. In the case of different  $C_s$  values and the dynamic subgrid model, the peak values at the two side walls were very similar, with the  $v_{rms}$  difference on the left side being only 0.003 m/s. Only at locations further away from the side walls did the results from the dynamic subgrid model align better with the experimental data. Similarly, for the vertical neutral line  $y$ , the variation of  $u_{rms}$  follows the same trend as  $v_{rms}$  along the neutral line  $x$ . When  $C_s = 0.18$  and using the dynamic subgrid model, the peak value errors at the top and bottom walls were small, with the error at the bottom wall side being only 0.01 m/s. Further away from the side walls, the velocity gradually decreased. When using the dynamic subgrid model, the peak

397 value of  $u_{rms}$  was much larger compared to the flow velocity interpolation at the vortex core,  
 398 with significant differences when  $C_s = 0.1$  and  $C_s = 0.18$ .



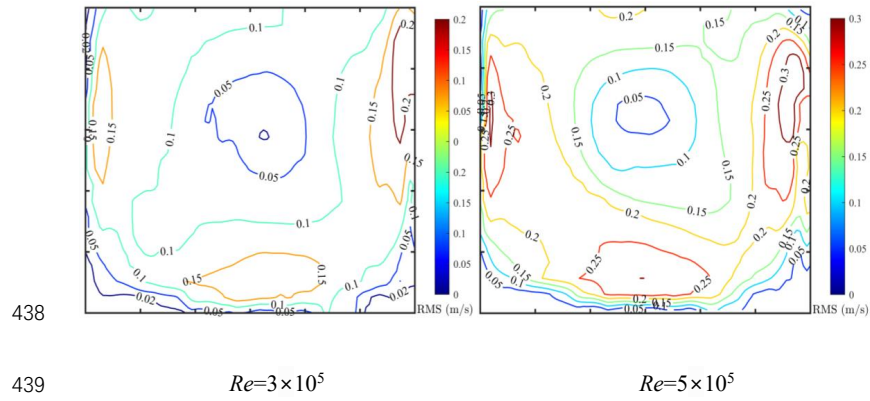
401 Figure 3: The vertical velocity along the neutral plane at  $Re = 10,000$ , as presented in  
 402 the data from Padilla and Martins (2005).

### 3.1.2 Flow Velocity on the Middle Plane

Figure 4 presents the distribution of the RMS velocity ( $w_{rms}$ ) on the middle plane ( $X=0$ ) under different Reynolds numbers ( $Re=3\times 10^5$ ,  $5\times 10^5$ ,  $7\times 10^5$ ,  $1\times 10^6$ ). Experimental results indicate a significant spatial non-uniformity in the RMS velocity across different flow conditions. The fluctuation intensity in the primary vortex core region is relatively low, whereas noticeable peaks in the RMS velocity appear in the near-wall regions, particularly along the downstream wall. Specifically, at  $Re=3\times 10^5$ , the maximum RMS velocity is approximately 0.24 m/s, and as the Reynolds number increases to  $1\times 10^6$ , the peak value rises to around 0.43 m/s, with the maximum always occurring near the downstream wall. This phenomenon may be attributed to the jet effect induced by the lid-driven flow, which generates a localized high shear region that leads to a sharp gradient in velocity near the right wall, forming a tightly spaced contour of velocity gradients. As the Reynolds number increases, the trend of increasing RMS velocity in the near-wall region becomes more pronounced, and the complexity of the contour distribution and shape also increases, further suggesting that at high Reynolds numbers, the spatial non-uniformity and dynamic evolution of turbulence fluctuations are enhanced. The increase in Reynolds number strengthens the inertial forces dominating the turbulent transport mechanism. In the near-wall region, the interaction between wall shear and the turbulent boundary layer intensifies the accumulation of velocity gradients and fluctuation energy, leading to a significant increase in RMS velocity with higher Reynolds numbers.

Specifically, at high Reynolds numbers, the frequency of turbulent vortex

breakdown and reorganization within the boundary layer increases, causing the fluctuation energy in the near-wall region to spread across a wider frequency range, thereby enhancing the local velocity fluctuation intensity. In contrast, the primary vortex core, being farther from the wall shear influence, exhibits higher flow stability. Therefore, the RMS velocity in this region is less dependent on Reynolds number. However, as the Reynolds number increases to  $1 \times 10^6$ , the turbulent mixing effects in the primary vortex region still lead to a slight increase in RMS velocity. This result highlights the competing mechanism between inertial and viscous forces in controlling the spatial distribution of turbulent energy. At high Reynolds numbers, the viscous dissipation effect near the walls weakens, and the inertial-dominated turbulent transport mechanism governs the distribution of energy. On the other hand, the core region is constrained by the momentum of the primary vortex structure, with its fluctuation evolution being dominated by local flow stability.



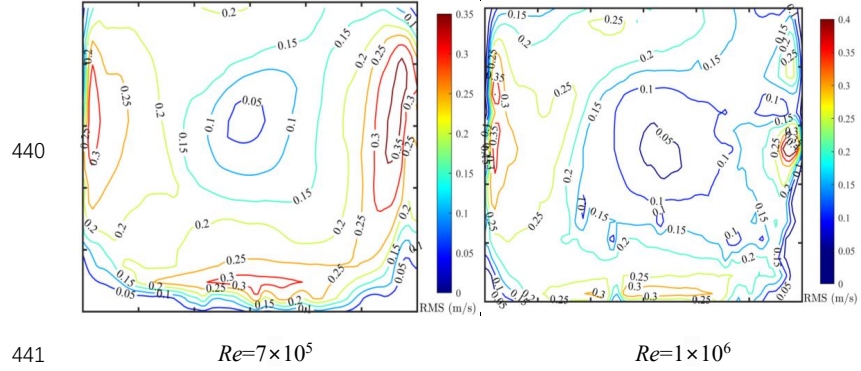


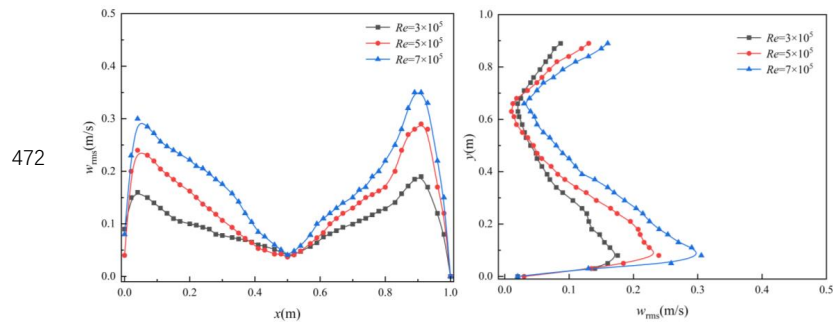
Figure 4: Root Mean Square Velocity on the Middle Plane

To gain deeper understanding of the distribution characteristics of the root mean square velocity ( $w_{rms}$ ) at different positions on the cavity's middleplane, Figure 5 shows the evolution of  $w_{rms}$  along the middle line and near the side wall lines ( $x=0.91, y=0.11$ ) under various conditions ( $Re=3\times10^5, 5\times10^5, 7\times10^5$ ). The experimental results indicate that the  $w_{rms}$  along the side wall near the cavity exhibits a typical single-peak distribution (Figure b). Starting from the side wall ( $x = 0, y = 0$ ), the  $w_{rms}$  gradually increases as the distance from the wall increases, reaching a peak near the core of the main vortex (at  $Re = 7\times10^5$ , the peak is approximately 0.37 m/s), and then gradually decays towards the opposite side wall. This phenomenon is attributed to the dynamic balance between the viscous effects in the near-wall region and turbulent energy transport. Near the wall, the viscous sublayer dampens the initial fluctuation intensity due to strong shear forces. As the distance from the wall increases (approximately  $x > 0.2$  or  $y > 0.2$ ), the viscous constraints weaken, and the inertial-dominated turbulent fluctuations rapidly accumulate, leading to a significant increase in  $w_{rms}$ . When the flow



reaches the main vortex region, the velocity reaches its maximum value. As the fluid continues to approach the wall ( $x > 0.6$  or  $y > 0.6$ ), the flow stabilizes, the momentum redistribution efficiency decreases, and the fluctuation energy dissipates gradually.

Notably, the  $w_{rms}$  distribution along the middle line exhibits a "bimodal" characteristic (Figure a). Specifically, the velocity near the side walls is relatively high (approximately 0.36 m/s), while the velocity in the main vortex core region ( $0.4 < x < 0.6$  or  $0.5 < y < 0.7$ ) significantly decreases to below 0.1 m/s. This difference arises from the momentum constraint effect of the main vortex structure on the flow in the core region, which suppresses the multi-scale evolution of turbulent fluctuations. In contrast, near the side walls, the shear layer instability and enhanced turbulent mixing significantly amplify the fluctuation characteristics. Further analysis shows that as the  $Re$  increases from  $3 \times 10^5$  to  $7 \times 10^5$ , the peak value of  $w_{rms}$  exhibits a systematic increase. The peak value at the main vortex position along the side wall line  $x = 0.91$  increases from 0.19 m/s at  $Re = 3 \times 10^5$  to 0.33 m/s at  $Re = 7 \times 10^5$ , while the  $w_{rms}$  along the side wall line  $y = 0.11$  increases from 0.18 m/s to 0.35 m/s.



(a) middle line

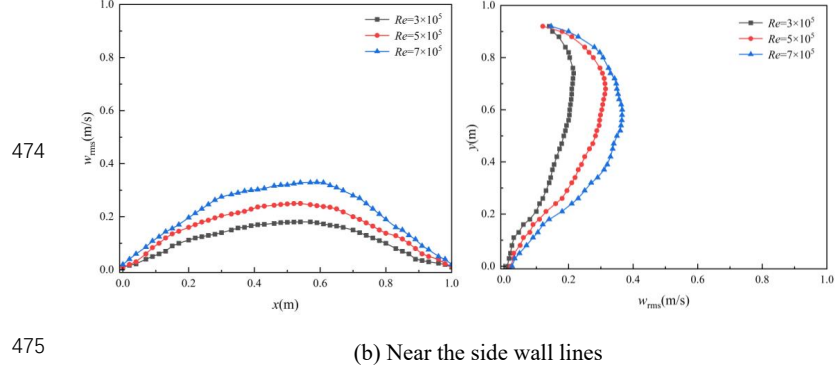


Figure 5: Root Mean Square Velocity at Different Locations on the Middle Plane

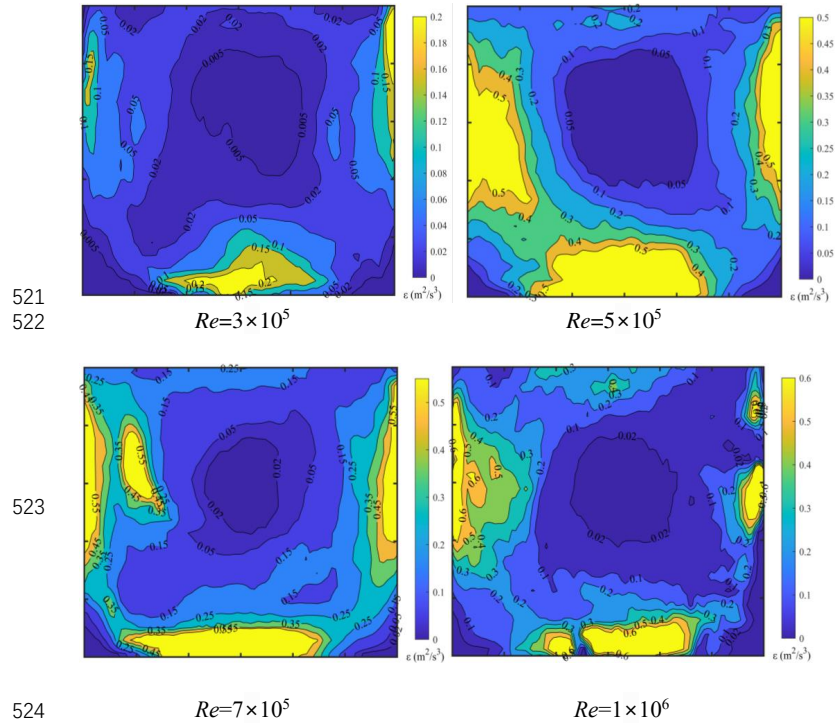
### 3.2 Dissipation Rate( $\varepsilon$ )

Figure 6 shows the spatial distribution of turbulence kinetic energy dissipation rates( $\varepsilon$ ) in the cavity at different Reynolds numbers ( $Re=3 \times 10^5$ ,  $5 \times 10^5$ ,  $7 \times 10^5$ ,  $1 \times 10^6$ ). The experimental results indicate significant spatial non-uniformity in the  $\varepsilon$ : the  $\varepsilon$  in the main vortex region is generally below 0.1, while in the near-wall regions (near the bottom and side walls), the  $\varepsilon$  increases substantially, with the peak reaching 0.6 at  $Re = 1 \times 10^6$ . As the Reynolds number increases from  $3 \times 10^5$  to  $1 \times 10^6$ , both the overall  $\varepsilon$  and its spatial complexity increase. Specifically, the  $\varepsilon$  near the bottom wall increases from 0.33 at  $Re = 3 \times 10^5$  to 0.68 at  $Re = 1 \times 10^6$ . At  $Re = 3 \times 10^5$ , the dissipation of turbulent kinetic energy is mainly concentrated near the wall, with the  $\varepsilon$  at the left side wall being only 0.15 and covering a small area. When the Reynolds number increases to  $5 \times 10^5$ , the  $\varepsilon$  increases significantly, and the high dissipation area expands. At  $Re = 7 \times 10^5$ , the high dissipation region at the left wall extends inward into the cavity, and two dissipation peak zones form on the left wall. At  $Re = 1 \times 10^6$ , the high dissipation regions

491 fragment, and multiple localized high dissipation zones appear on the bottom and side  
492 walls, with the contour lines evolving from continuous bands to multi-scale fragmented  
493 structures, reflecting the dynamic evolution of the turbulence multi-scale vortex  
494 structures.

495       The near-wall regions experience high dissipation rates due to the boundary layer,  
496 where the velocity gradient is steepened by wall shear. In these regions, viscous  
497 dissipation dominates the energy loss, leading to a significant increase in the local  
498 dissipation rate. As the Reynolds number increases, turbulence fluctuations dominated  
499 by inertial forces enhance, making the flow more prone to turbulence and vortex  
500 formation. The interaction, stretching, and breaking of these vortices cause rapid energy  
501 dissipation, leading to an increase in the dissipation rate. In the near-wall regions, the  
502 turbulence activity within the boundary layer intensifies as Reynolds number increases,  
503 enhancing viscous dissipation and thus increasing the dissipation rate. Moreover, at  
504 high Reynolds numbers, the flow instability intensifies, leading to the emergence of  
505 smaller-scale vortex structures within the cavity, further enhancing energy dissipation.  
506 A comparison with Samantaray et al.(2019) in their study of cavity flows at  $Re \leq$   
507  $1.5 \times 10^4$  reveals a common trend of significant increases in dissipation rates near the  
508 wall. This study further shows that the high dissipation regions extend from near the  
509 wall into the cavity as Reynolds number increases, and more regions inside the cavity  
510 show a significant rise in turbulence dissipation rates, with more intense changes in  
511 contour lines. Additionally, Gnanasekaran and Satheesh (2024) found in their numerical  
512 study of turbulence in double-cavity flows that, under specific length-to-width and

513 velocity ratio conditions, the dissipation rate may decrease as the Reynolds number  
 514 increases. This phenomenon is likely related to the geometric configuration of the  
 515 double cavity and its effect on the stability of the main vortex structure, which may  
 516 inhibit the development of turbulence and thus weaken energy dissipation. The results  
 517 of this study show that, in a single-sided driven cavity, the positive reinforcing effect of  
 518 Reynolds number on dissipation rates dominates, further highlighting the significant  
 519 influence of geometric configuration and driving conditions on turbulence dissipation  
 520 mechanisms.



525 Figure 6: Distribution of dissipation Rate.

### 526 3.3 Smagorinsky Constant

527 Figure 7 shows the distribution of the Smagorinsky constant in the cavity at  
528 different Reynolds numbers ( $Re=3\times 10^5$ ,  $5\times 10^5$ ,  $7\times 10^5$ ,  $1\times 10^6$ ). At each Reynolds  
529 number, the Smagorinsky constant exhibits a distinct non-uniform distribution within  
530 the cavity. In the boundary regions, the value is relatively small. Starting from the  
531 boundary, as the distance from the wall increases, the constant first increases and then  
532 decreases. The region closest to the boundary is where turbulence and viscosity are the  
533 most intense, and the Smagorinsky constant reaches its maximum value. In the central  
534 primary vortex region, which is essentially in the laminar range (no viscosity), the  
535 Smagorinsky constant increases from 0.02 m/s at  $Re=3\times 10^5$  to 0.05 m/s at  $Re=1\times 10^6$ ,  
536 and is close to zero. The turbulence characteristics at different positions within the  
537 cavity show significant variations, resulting in corresponding changes in the  
538 Smagorinsky constant used for simulating subgrid-scale stresses. Notably, although the  
539 Smagorinsky constant is larger near the boundary, the exact values for different walls  
540 vary. The bottom wall has a larger value than the top wall, with the maximum value  
541 often appearing in the upstream region, mainly concentrated near the upstream area of  
542 the UUV region.

543 As the Reynolds number increases, the maximum value of the Smagorinsky  
544 constant within the cavity also increases. The maximum value at  $Re=3\times 10^5$  is around  
545 0.3, reaching 0.35 at  $Re=5\times 10^5$ , 0.4 at  $Re=7\times 10^5$ , and 0.6 at  $Re=1\times 10^6$ . This trend  
546 indicates that the increase in Reynolds number strengthens the turbulence within the  
547 cavity, leading to an increase in eddy viscosity, which is reflected in the rise of the

548 maximum value of the Smagorinsky constant. Additionally, although the overall  
549 distribution trend remains unchanged, at higher Reynolds numbers, the region with  
550 higher values of the constant expands, indicating that Reynolds number influences both  
551 the distribution range and intensity of the Smagorinsky constant within the cavity.  
552 Furthermore, as the Reynolds number increases, the turbulence within the cavity  
553 intensifies, and the region of the Smagorinsky constant tends to break up more, with  
554 the contour lines becoming more complex and the gradients steeper.

555       From the perspective of turbulence theory, near solid boundaries or in other  
556 laminar regions, turbulence-generated viscosity is zero, resulting in the Smagorinsky  
557 constant of zero. Closer to the boundary, the fluid is influenced by the wall, leading to  
558 complex state with strong turbulence, and a larger Smagorinsky constant is required to  
559 accurately simulate the subgrid-scale stresses and energy transfer. In the intermediate  
560 primary vortex region, which is in the laminar range and has no viscosity, the  
561 Smagorinsky constant decreases to zero (Kresta and Wood,1993). As the Reynolds  
562 number increases, the relative strength of inertial forces over viscous forces increases,  
563 and the turbulence intensity escalates. The number and activity of small-scale vortices  
564 increase, and to better simulate the subgrid-scale effects at this high turbulence intensity,  
565 the maximum value of the Smagorinsky constant increases accordingly. In conclusion,  
566 using a constant Smagorinsky value throughout the entire flow in high Reynolds  
567 number large eddy simulations is inaccurate. Since eddy viscosity differs across  
568 different regions of the flow, the corresponding Smagorinsky constant should also adapt  
569 accordingly.

570 The experimental findings of this study reveal the spatial correlation between the  
 571 Smagorinsky constant and turbulence characteristics in high-Reynolds lid-driven cavity  
 572 flows, providing the following physical basis for the optimization of subgrid-scale  
 573 models: Experimental data show that  $C_s$  exhibits a non-uniform distribution  
 574 approaching zero in the boundary wall region ( $C_s \approx 0$  at  $Re = 1 \times 10^6$ ). Its value  
 575 increases and then decreases with increasing distance from the wall, and the peak  
 576 position is significantly correlated with the spatial distribution of the local turbulent  
 577 kinetic energy dissipation rate. Further analysis shows that the peak value of  $C_{smax}$   
 578 increases with Reynolds number, from 0.3 at  $Re = 3 \times 10^5$  to 0.6 at  $Re = 1 \times 10^6$ . This  
 579 suggests that subgrid models need to introduce Reynolds number-dependent dynamic  
 580 scaling relationships (such as  $C_s \propto Re^{-\nu}$ ) to match the energy cascade process dominated  
 581 by inertial effects. In addition, the spatial non-uniformity of the turbulent kinetic  
 582 energy dissipation rate (with peak values near the wall reaching 0.6 and below 0.1 in  
 583 the core region) indicates that the model must achieve a refined calibration of the  
 584 dissipation term by dynamically relating  $C_s$  with local flow parameters (e.g., wall  
 585 distance  $y^+$ ), particularly in the near-wall high shear region, where enhanced dissipation  
 586 resolution is needed to suppress excessive damping effects, where the near-wall  $v_{rms}$   
 587 error reaches 0.03 m/s at  $C_s = 0.18$ ). Notably, the low sensitivity of  $u_{rms}$  to Reynolds  
 588 number in the primary vortex core (variation  $< 0.1$  m/s) provides a validation benchmark  
 589 for the robustness of the model in the inertial-dominated region. Compared to the  
 590 fixed  $C_s$  model, the dynamic model reduces the error in this region to 0.01 m/s,  
 591 confirming the superiority of the spatially adaptive  $C_s$  distribution. These findings

provide experimental support for the development of partitioned dynamic subgrid  
models. Future research could further optimize the near-wall model parameterization  
by incorporating the quantitative relationship between local dissipation rate and  $C_s$ .

595

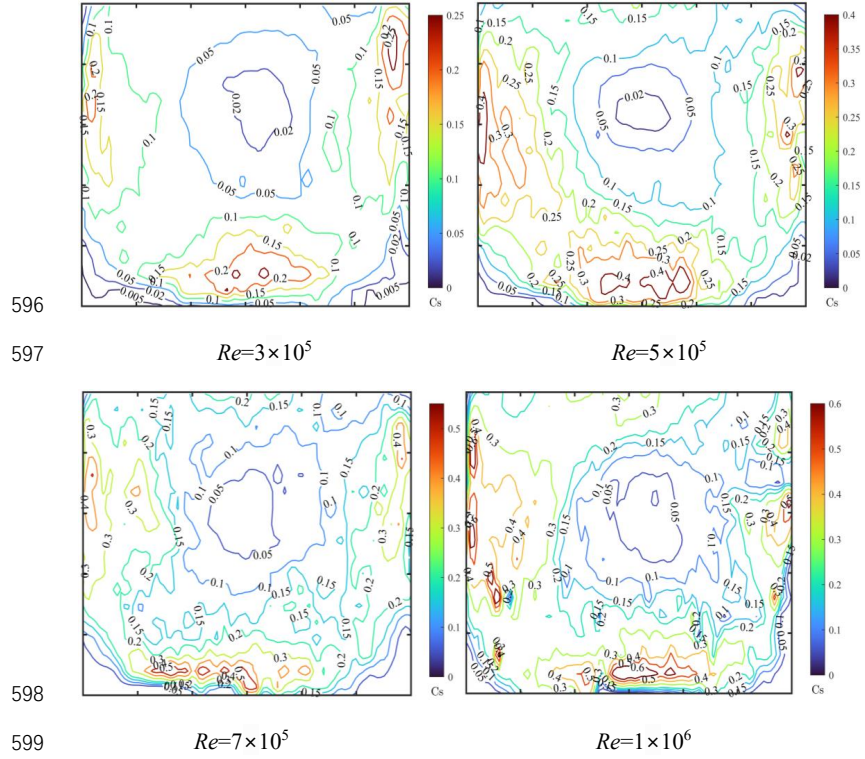


Figure 7: Distribution of the Smagorinsky constant

#### 4. Conclusions

This study examined water flow dynamics in a lid-driven cavity under four high  
Reynolds number conditions:  $Re = 3 \times 10^5$ ,  $5 \times 10^5$ ,  $7 \times 10^5$ , and  $1 \times 10^6$ . The flow field



604 within the cavity was measured using PIV, and RMS velocities and turbulent kinetic  
605 energy dissipation rates within the cavity were calculated. Using combination of the  
606 dimensional analysis method and large eddy PIV method, the distribution of the  
607 Smagorinsky constant within the cavity was further determined. The experimental  
608 findings yield the following key conclusions:

609 (1) Variation of RMS Velocity: As the Reynolds number increases, the RMS  
610 velocities ( $u_{rms}$  and  $v_{rms}$ ) in the near-wall region of the cavity increase significantly,  
611 especially near the downstream wall where the RMS velocity reaches its peak. This  
612 indicates that, under high Reynolds number conditions, the turbulence intensity in the  
613 wall-adjacent regions is amplified. Specifically, when  $Re$  increases from  $3 \times 10^5$  to  $1 \times 10^6$ ,  
614 the RMS velocity at the bottom wall increases from 0.19 m/s to 0.35 m/s, further  
615 highlighting the significant increase in turbulence intensity in the boundary layer under  
616 high Reynolds number flows.

617 (2) The turbulent kinetic energy dissipation rate distribution on the neutral plane  
618 of the cavity, obtained using both dimensional analysis and large eddy PIV methods,  
619 reveals higher dissipation rate near the left and right cavity walls. Moreover, under high  
620 Reynolds number conditions, the dissipation rate exhibits clear spatial non-uniformity.  
621 As the Reynolds number increases, the overall dissipation rate level rises, particularly  
622 in the near-wall region, where the dissipation of turbulent kinetic energy becomes  
623 significantly higher. For example, at  $Re = 1 \times 10^6$ , the peak dissipation rate near the  
624 bottom wall reaches 0.6, with its influence extending further within the cavity. These  
625 findings suggest that as the Reynolds number increases, the inertial forces dominate the

626 turbulent fluctuations, causing more intense dissipation of turbulent energy, which  
627 highlights the increased turbulent intensity and the spatial complexity of energy  
628 dissipation at high Reynolds numbers.

629 (3) Smagorinsky Constant Distribution: The Smagorinsky constant calculated  
630 from the experimental results is close to zero near the cavity walls and gradually  
631 increases with distance from the wall, reaching a maximum value before decreasing to  
632 zero in the central region of the cavity. As the Reynolds number increases, the  
633 Smagorinsky constant also rises, especially at higher Reynolds numbers, where the  
634 enhanced vortex viscosity leads to a higher peak value of the Smagorinsky constant.

635 Limitations: It is important to note that this study was conducted using a 2D plane  
636 for the experimental setup, and the results may not fully capture the complexities of  
637 three-dimensional flow dynamics. Testing 3D models could provide further insights  
638 into the flow behavior and energy dissipation mechanisms in the cavity, particularly at  
639 higher Reynolds numbers. This aspect will be considered as a direction for future  
640 research.

#### 641 **Acknowledgements**

642 This study is supported by the Qin Chuang Yuan high-level innovation and  
643 entrepreneurship talent project (No: QCYRCXM2023-099), the 2024 major projects to  
644 prevent and control sand demonstration ‘Unveiled Marshal’ project from the Inner  
645 Mongolia Department of Science and Technology (No: 2024JBGS0016), the National  
646 Foreign Experts Individual Program (Category H) under national funding (No:

647 H20240398) , and the Xianyang Science and Technology Bureau (No: L2024-ZDYF-  
648 ZDYF-SF-0042).

## 649 **References**

- 650 Beck, A., Flad, D., Munz, C. D., 2019. Deep neural networks for data-driven LES  
651 closure models. *Journal of Computational Physics*, 398, 108910.  
652 <https://doi.org/10.1016/j.jcp.2019.108910>.
- 653 Bianco, V., Cossu, R., Guarini, M., 2016. A comparison of the application of RSM and  
654 LES turbulence models in the numerical simulation of thermal and flow patterns in a  
655 double-circuit Ranque-Hilsch vortex tube. *Applied Thermal Engineering*, 106, 1244-  
656 1256. <https://doi.org/10.1016/j.applthermaleng.2016.06.024>.
- 657 Buaria, D., Sreenivasan, K. R. (2020). Dissipation range of the energy spectrum in high  
658 Reynolds number turbulence. *Physical Review Fluids*, 5(9), 092601(R).  
659 <https://doi.org/10.1103/PhysRevFluids.5.092601>
- 660 de Crouy-Chanel, M., Bouffanais, R., Leriche, E., 2024. Large-Eddy Simulations with  
661 remeshed Vortex methods: An assessment and calibration of subgrid-scale models.  
662 *Computers and Fluids*, 277, 106287. <https://doi.org/10.1016/j.compfluid.2024.106287>.
- 663 Germano, M., Piomelli, U., Moin, P., Cabot, W. H., 1991. A dynamic subgrid-scale eddy  
664 viscosity model. *Physics of Fluids A*, 3(7), 1760-1765.  
665 <https://doi.org/10.1063/1.857955>.
- 666 Geurts, B. J., Meyers, J. N., Geier, M., 1999. Dynamic subgrid-scale modeling of  
667 turbulent scalar transport. *Physics of Fluids*, 11(8), 2527-2540.

668 <https://doi.org/10.1063/1.870113>.

669 Ghia, U., Ghia, K. N., Shin, C. T., 1982. High-Re solutions for incompressible flow  
670 using the Navier-Stokes equations. *Journal of Computational Physics*, 48(3), 387-411.  
671 [https://doi.org/10.1016/0021-9991\(82\)90058-4](https://doi.org/10.1016/0021-9991(82)90058-4).

672 Kresta, S. M., Wood, P. E. (1993). The flow field produced by a pitched blade turbine:  
673 Characterization of the turbulence and estimation of the dissipation rate. *Chemical*  
674 *Engineering Science*, 48(10), 1761-1774. [https://doi.org/10.1016/0009-2509\(93\)803](https://doi.org/10.1016/0009-2509(93)80346-R)  
675 46-R.

676 Ling, J., Kurzawski, A., Templeton, J., 2016. Reynolds averaged turbulence modelling  
677 using deep neural networks with embedded invariance. *Journal of Fluid Mechanics*,  
678 807, 155-166. <https://doi.org/10.1017/jfm.2016.635>.

679 Malik, S., Sharma, S., Sharma, M., 2016. Shear improved Smagorinsky model for large  
680 eddy simulation of flow in a stirred tank with a Rushton disk turbine. *Chemical*  
681 *Engineering Research and Design*, 108, 69-80.  
682 <https://doi.org/10.1016/j.cherd.2016.06.002>.

683 Meneveau, C., & Katz, J. (2000). Scale-Invariance and Turbulence Models for Large-  
684 Eddy Simulation. *Annual Review of Fluid Mechanics*, 32, 1-32. [https://doi.org/1](https://doi.org/10.1146/annurev.fluid.32.1.1)  
685 [0.1146/annurev.fluid.32.1.1](https://doi.org/10.1146/annurev.fluid.32.1.1)

686 Nicoud, F., Ducros, F., 1999. Subgrid-scale stress modelling based on the square of the  
687 velocity gradient tensor. *Flow, Turbulence and Combustion*, 62(3), 183-200.  
688 <https://doi.org/10.1023/A:1009995426001>.

689 Pan, F., Acrivos, A., 1967. Steady flows in rectangular cavities. *Journal of Fluid*

690 Mechanics, 28(4), 643-655. <https://doi.org/10.1017/S0022112067002283>.

691 Piomelli, U., Balaras, E., 2002. Wall-layer models for large-eddy simulations. Annual  
 692 Review of Fluid Mechanics, 34, 349-374. <https://doi.org/10.1146/ann>  
 693 urev.fluid.34.082701.144216.

694 Smagorinsky, J., 1963. General circulation experiments with the primitive equations.  
 695 Monthly Weather Review, 91(3), 99-164. <https://doi.org/10.1175/1520->  
 696 0493(1963)091<0099:GCEWTP>2.3.CO;2.

697 Spalart, P. R., Allmaras, S. R., 2006. A new version of detached-eddy simulation.  
 698 Theoretical and Computational Fluid Dynamics, 20(3), 181-195.  
 699 <https://doi.org/10.1007/s00162-006-0015-0>.

700 Vreman, A. W., Geurts, B. J., Kuerten, H. J., 2004. An eddy-viscosity subgrid-scale  
 701 model for turbulent shear flow. Physics of Fluids, 16(10), 3670-3681.  
 702 <https://doi.org/10.1063/1.1785131>.

703 Bertolini, E., Pieringer, P., Sanz, W., 2021. Large Eddy Simulation of a Transonic Linear  
 704 Cascade With Synthetic Inlet Turbulence. ASME Turbo Expo 2020: Turbomachinery  
 705 Technical Conference and Exposition. <https://doi.org/10.1115/GT2020-14461>.

706 Tennekes, H., Lumley, J. L., 1972. A first course in turbulence. MIT Press.

707 Kresta, S. M., Wood, P. E., 1993. The flow field produced by a pitched blade turbine:  
 708 characterization of the turbulence and estimation of the dissipation rate. Chemical  
 709 Engineering Science, 48, 1761-1774. [https://doi.org/10.1016/0009-2509\(93\)80139-5](https://doi.org/10.1016/0009-2509(93)80139-5).

710 Sikiö, P., Tynjälä, T., Jalali, P., 2018. Turbulent energy dissipation rate modification due  
 711 to particle insertion: Effect of Reynolds number. Chaos, Solitons and Fractals, 114, 246-

255. <https://doi.org/10.1016/j.chaos.2018.06.038>.

Sheng, J., Meng, H., Fox, R. O., 2000. A large eddy PIV method for turbulence dissipation rate estimation. *Chemical Engineering Science*, 55(20), 4423-4434. [https://doi.org/10.1016/S0009-2509\(00\)00234-9](https://doi.org/10.1016/S0009-2509(00)00234-9).

Arun, R., Bae, H. J., McKeon, B. J., 2023. Towards real-time reconstruction of velocity fluctuations in turbulent channel flow. *Physical Review Fluids*, 8(6), 064612. <https://doi.org/10.1103/PhysRevFluids.8.064612>.

Fan, B., Wang, Y., Yuan, Z., Wang, J., 2024. Eddy viscosity enhanced temporal direct deconvolution model for temporal large-eddy simulation of turbulent channel flow. *Physics of Fluids*, 36(6). <https://doi.org/10.1063/5.0233668>.

Prasad, A., Koseff, J., 1989. Reynolds number and end-wall effects on a lid-driven cavity flow. *Physics of Fluids A: Fluid Dynamics*, 1(2). <https://doi.org/10.1063/1.857492>.

Samantaray, D., Das, M. K., Patel, D. K., 2020. Turbulence characteristics of high Reynolds number flow inside a three-dimensional cubic lid-driven cavity. *European Journal of Mechanics - B/Fluids*, 84, 23 – 39. <https://doi.org/10.1016/j.euromechflu.2020.05.009>.

Padilla, E. L. M., Martins, A. L., Silveira-Neto, A., 2005. Large-eddy simulation of the three-dimensional unstable flow in a lid-driven cavity. *Proceedings of COBEM 2005: 18th International Congress of Mechanical Engineering, ABCM*.

Samantaray, D., Das, M. K., 2019. Nature of turbulence inside a cubical lid-driven cavity: Effect of Reynolds number. *International Journal of Heat and Fluid Flow*, 80,

734 108498. <https://doi.org/10.1016/j.ijheatfluidflow.2019.108498>.

735 Gnanasekaran, M., Satheesh, A., 2024. Numerical analysis of turbulent flow  
 736 characteristics with the influence of speed ratio in a double-sided cavity. *MethodsX*, 12,  
 737 102594. <https://doi.org/10.1016/j.mex.2024.102594>.

738 Shankar, P. N., Deshpande, M. D., 2000. Fluid mechanics in the driven cavity. *Annual*  
 739 *Review of Fluid Mechanics*, 32(1), 93-136. <https://doi.org/10.1146/annurev.flu>  
 740 [id.32.1.93](https://doi.org/10.1146/annurev.flu.id.32.1.93).

741 Padilla, M., Leibsohn Martins, A., da Silveira-Neto, A., 2005. Large-eddy simulation  
 742 of the three-dimensional unstable flow in a lid-driven cavity. *Proceedings of COBEM*  
 743 *2005*, 18th International Congress of Mechanical Engineering, November 6-11, Ouro  
 744 Preto, MG.

745 Piomelli, U., Liu, C., 1995. Wall-adapted local eddy-viscosity models for near-wall  
 746 turbulent flows. *AIAA Journal*, 33(11), 2086-2093. <https://doi.org/10.2514/3.12185>.

747 Wang, P., Peng, Y., Cheng, S., Gao, L., Yin, X., Shen, Y., Gao, X., 2025. Cavity flows  
 748 at high Reynolds numbers. *Physics of Fluids*, 37(3), 035146. [https://doi.org/1](https://doi.org/10.1063/5.0256965)  
 749 [0.1063/5.0256965](https://doi.org/10.1063/5.0256965).